MOLECULAR IMAGING AND BIOLOGY

Mol Imaging Biol (2013) 15:384–390
DOI: 10.1007/s11307-013-0626-y

Published Online: 19 March 2013

World Molecular Imaging Society

BRIEF ARTICLE

Whole-Body Biodistribution and Radiation Dosimetry of the Cannabinoid Type 2 Receptor Ligand [^{11}C]-NE40 in Healthy Subjects

Rawaha Ahmad,[1] Michel Koole,[1] Nele Evens,[2] Kim Serdons,[2] Alfons Verbruggen,[2] Guy Bormans,[2] Koen Van Laere[1]

[1]*Division of Nuclear Medicine, University Hospital Leuven, Herestraat 49, 3000, Leuven, Belgium*
[2]*Laboratory for Radiopharmacy, University Hospital Leuven, KU Leuven, Leuven, Belgium*

Abstract

Purpose: The type 2 cannabinoid receptor (CB2R) is part of the human endocannabinoid system and is involved in central and peripheral inflammatory processes. *In vivo* imaging of the CB2R would allow study of several (neuro)inflammatory disorders. In this study we have investigated the safety and tolerability of [^{11}C]-NE40, a CB2R positron emission tomography (PET) ligand, in healthy human male subjects and determined its biodistribution and radiation dosimetry.

Procedure: Six healthy male subjects (age 20–65 years) underwent a dynamic series of nine whole-body PET/CT scans for up to 140 min, after injection of an average bolus of 286 MBq of [^{11}C]-NE40. Organ absorbed and total effective doses were calculated through OLINDA.

Results: [^{11}C]-NE40 showed high initial uptake in the spleen and a predominant hepatobiliary excretion. In the brain, rapid uptake and swift washout were seen. Organ absorbed doses were largest for the small intestine and liver, with 15.6 and 11.5 μGy/MBq, respectively. The mean effective dose was 3.64±0.81 μSv/MBq. There were no changes with aging observed. No adverse events were encountered.

Conclusions: This first-in-man study of [^{11}C]-NE40 showed an expected biodistribution compatible with lymphoid tissue uptake and appropriate fast brain kinetics in the healthy human brain, underscoring the potential of this tracer for further application in central and peripheral inflammation imaging. The effective dose is within the typical expected range for ^{11}C ligands.

Key words: Biodistribution, Dosimetry, Positron emission tomography, [^{11}C]-NE40, CB2R

Introduction

The type 2 cannabinoid receptor (CB2R), isolated and structurally characterized in the early 1990s of the past century [1], is part of the endocannabinoid system (ECS), together with the type 1 (CB1R) receptor. Both the cannabinoid CB1R and CB2R are G protein-coupled receptors (GPCRs) that are quite divergent in structure with only 44 % overall homology [2]. In contrast to the CB1R, which is the most abundant GPCR in the central nervous system (CNS), the CB2R is widely expressed in immune-related tissues and organs, with high expression levels in the spleen, tonsils, and leucocytes [3]. Outside the immune system, CB2R is expressed to a lesser extent in the salivary gland, skeletal muscle, pancreas, ovary, and testis [4–8]. In non-pathological conditions, cerebral CB2R expression is very low and only present in the cerebellum and pons [9, 10]. CB2Rs are upregulated in inflammatory conditions by activated microglia and involved in the production of nitric oxide and cytokines [11]. Furthermore, the CB2R is involved in pain processing [12].

Correspondence to: Rawaha Ahmad; *e-mail:* rawaha.ahmad@uzleuven.be

There is accumulating evidence that the ECS is involved in the pathogenesis and clinical expression of neurodegenerative disorders, in part through the process of neuroinflammation [13, 14]. Upregulation of CB2R has been described post-mortem in patients with Alzheimer's disease [15], Huntington's disease, [16] and Parkinson's disease [17]. Therefore, positron emission tomography (PET) imaging of CB2R in the CNS can provide a tool to investigate the *in vivo* importance of CB2R in central inflammatory disorders.

Whereas several PET radioligands have been validated for the CB1R [18–20], only more recent attempts to radiolabel probes for CB2R have been undertaken [21]. A carbon-11-labeled CB2-selective PET tracer was described but without penetration of the blood–brain barrier [22, 23], limiting its applicability to peripheral visualization of the CB2R. Recently, we have developed and validated a novel specific radioligand for CB2R PET, 2-oxo-7-[^{11}C]-methoxy-8butyloxy-1,2-dihydroquinoline-3-carboxylic acid cyclohexylamide ([^{11}C]-NE40). This PET ligand is fairly lipophilic (logarithmic distribution coefficient of 3.9 and total polar surface area of 80.42 Å^2) [24]. *In vitro* ligand binding studies using Chinese hamster ovary cells expressing the human CB2R have shown that NE40 has a relatively high binding affinity (Ki=9.6 nM), which was confirmed by *in vivo* CB2R binding in mouse spleen [22, 24], and high specificity (100-fold over the CB1R). Radioligand safety was investigated by toxicity studies including genotoxicity (Ames test) and histopathologic evaluation in rats [25] under the microdosing concept [26]. *In vivo* binding in a rat model with adeno-associated viral human CB2R overexpression was confirmed [27]. Here we describe the first-in-man imaging studies, with safety and dosimetry assessment in both young and elderly male volunteers.

Materials and Methods

Subjects

Healthy subjects were recruited in response to an advertisement in a local community newspaper. Six healthy Caucasian male subjects were included in the study. Table 1 shows the demographic data. The subjects did not have any clinically significant medical or neurological history, and they did not have any clinically significant abnormality on physical, neurological, or laboratory examinations. In addition, they were not taking any anti-inflammatory medication at the moment of the scan or during at least 4 weeks before the scan. The study was approved by the local ethics committee and conducted according to the latest guidelines of the Declaration of Helsinki. Written informed consent was obtained from all volunteers before the start of their study.

Radiotracer Characteristics and Preparation of [^{11}C]-NE40

Radiotracer preparation was performed as described previously [24]. In short, a stream of helium containing [^{11}C]-CH_3I was bubbled through a solution of 200 µg 2-oxo-7-hydroxy-8-butyloxy-1,2-dihydroquinoline-3-carboxylic acid cyclohexylamide and 2–4 mg Cs_2CO_3 in 200 µl dimethylformamide. The reaction mixture was heated and diluted. The radiolabeled compound [^{11}C]-NE40 was collected using reversed-phase high-performance liquid chromatography (HPLC). After formulation, the identity and the chemical and radiochemical purity of the tracer agent [^{11}C]-NE40 were checked using HPLC. Specific activity was 363 GBq/µmol (range 200–632); the maximum amount of cold NE40 injected was <1.0 µg (range 0.4–0.9).

PET/CT Procedure

All subjects fasted for at least 6 h before PET. Subjects underwent a dynamic series of nine whole-body (WB) PET–CT scans on a Hirez Biograph 16 PET/CT (Siemens, Erlangen, Germany) after bolus I.V. injection of 286 MBq (range 201–325 MBq) of [^{11}C]-NE40. Data were acquired with a single energy window set at 425 to 650 keV. The first PET segment (sequential acquisition of WB scans 1 to 8) started simultaneously with the bolus injection and lasted for 60 min (time per bed position 30 s (for WB1–3), 60 s (for WB4–6), and 120 s (for WB7 and WB8)). The second segment (WB9) started at 120 min post-injection at 4 min per bed position. A low-dose CT (tube potential 80 kV; 11 mAs) was performed before each scan segment (the additional effective dose from this CT is 0.5 mSv (CT-Expo version 1.7, male phantom), so the subject underwent an estimated additional radiation burden of 1.0 mSv on top of the PET study). At our center, daily quality control of the PET system is performed using a uniform ^{68}Ge cylinder to check the uniformity and the stability of the system. Cross calibration with the dose calibrator is performed at least every 3 months using a uniform ^{18}F cylinder. Whole-body images were reconstructed using a three-dimensional ordered subset expectation maximization iterative reconstruction, with five iterations and eight subsets, with CT-based attenuation and scatter correction by standard vendor-based reconstruction. No partial volume effect correction was performed.

Urine was collected after each scan segment for total urinary bladder activity determination and up to 3 h post-injection. Volume was determined by weighing the amount of urine, and activity concentration was determined by measuring the activity of a defined volumetric sample of 1 ml with a well counter (Wallac 1480 wizard 14 in., PerkinElmer, Turku, Finland).

Safety was assessed through physical and neurological examination, vital parameter assessment, electrocardiogram

Table 1. Subject data, net injected activity of [^{11}C]-NE40, and individual effective dose

Subject	Sex	Age (y)	Height (cm)	Mass (kg)	Body mass index (kg/m^2)	Injected activity (MBq)	Individual ED (μSv/MBq)
HV_1	M	20.8	178	61	19.3	302.3	3.93
HV_2	M	44.9	187	90	25.7	201.2	2.79
HV_3	M	24.2	186	86	24.8	254.8	3.05
HV_4	M	65.3	166	61	22.1	310.1	5.09
HV_5	M	61.0	187	90	25.7	324.1	3.46
HV_6	M	22.6	192	82	22.2	325.8	3.54
Mean±SD		39.8±20.1	182.7±9.3	78.3±13.8	23.3±2.6	286±49	3.64±0.81

HV healthy volunteer, *M* male, *y* year, *SD* standard deviation, *ED* effective dose

(ECG), laboratory testing, and monitoring of subjective adverse experiences with telephone follow-up 24 h and 14 days post-injection.

Data Analysis

Data were analyzed and reported according to the EANM guidelines for clinical dosimetry reporting [28]. Reconstructed data were analyzed using PMOD software (version 3.0; PMOD Inc., Zurich). Three-dimensional volumes of interest (VOIs) were constructed on the PET emission images to include all organ activity, and their position was verified on corresponding CT images, as described previously [29]. The following organs with significant visualized activity were included as source organs: brain, gallbladder, intestines, heart, kidneys, liver, lungs, red marrow, spleen, thyroid, and urinary bladder. Total tracer retention as a function of time or time–activity curves (TACs) was determined. Each whole body is scanned in different bed positions, hereby creating a difference in timing for each organ. Therefore, we calculated the acquisition time for every organ by looking at the organ's axial midposition on the corresponding CT scout image and checked at which bed position the spatial overlap was observed. For the axial red marrow, we took the average time value of the midlumbar vertebral position. In this way, we calculated time–activity curves for all the source organs.

To determine preliminary kinetics of brain and spleen uptake, mean standard uptake value (SUV) TACs for the brain and spleen were generated.

Organ time-integrated activity coefficients (previously named "residence times" [30]) were computed by calculating the area under the TAC of each source organ through curve fitting. Different models for different organs were used, depending on their kinetics (standardly, a bi-exponential curve was taken when the first data point was already the maximum activity point; in other cases, an extra factor or term $(1-\exp(-\ln(2)\times T/T_i))$ was included to produce a better fit with a specific maximum). For the heart wall, kidneys, spleen, and thyroid, a bi-exponential was fitted, while a mono-exponential could be used for the lungs. To account for the tracer uptake phase in the brain and liver, the function $A_1\times(1-\exp(-\ln(2)\times T/T_1))\times\exp(-\ln(2)\times T/T_2)$ was fitted to the TAC, while the function $A_1\times(1-\exp(-\ln(2)\times T/T_1))\times\exp(-\ln(2)\times T/T_2)+A_2\times\exp(-\ln(2)\times T/T_{e3})$ was used to model the TAC of the gallbladder, red marrow, and remainder.

The International Commission on Radiological Protection (ICRP) 30 gastrointestinal (GI) model [31] was used to determine the time-integrated activity coefficients for the organs involved in the gastrointestinal tract, while the voiding bladder model with a voiding interval of 2 h was used to estimate the time-integrated activity coefficient for the urinary bladder (UB) [32]. The fraction of injected activity entering the small intestines was estimated by fitting the exponential $A_{GI1}+A_{GI2}\times(1-\exp(-\ln(2)\times T/T_{GI}))$ to the decay-corrected TAC of the intestinal VOI. Total fraction for the gastrointestinal tract was determined as $(A_{GI1}+A_{GI2})$ normalized to injected activity A_{inj}. The remaining fraction of the injected activity was considered as excreted through the urinary bladder. Biological half-life for the fraction entering the urinary bladder was estimated by fitting $(A_{inj}-A_{GI1}-A_{GI2})\times(1-\exp(-\ln(2)\times T/T_{UB}))$ to the TAC of the urinary bladder corrected for decay and between scan voiding. Radiation exposure of the body and critical organs was calculated from the tracer time-integrated activity coefficients using the OLINDA (Organ Level Internal Dose Assessment, Vanderbilt University, USA) software package. The effective dose (ED) was calculated from the individual organ doses with a predefined weighting factor for each of the source organs [33].

Results

As for safety, all monitored clinical parameters (heart rate, blood pressure, 12-lead electrocardiogram, blood analysis) remained normal, and no clinically significant adverse experiences were reported by the subjects at the time of scanning, nor were any reported during the follow-up phone interviews.

Figure 1 shows a series of coronal and sagittal whole-body slices of [^{11}C]-NE40 over time for a representative subject. The tracer was readily taken up in the liver and partially excreted through the gastrointestinal system. Some urinary tract activity was noted after a few minutes. Based on the statistics of the abdominal VOI, 10.5±7.5 % of the injected activity was entering the intestines and therefore considered as hepatobiliary clearance. The remaining fraction was considered excreted

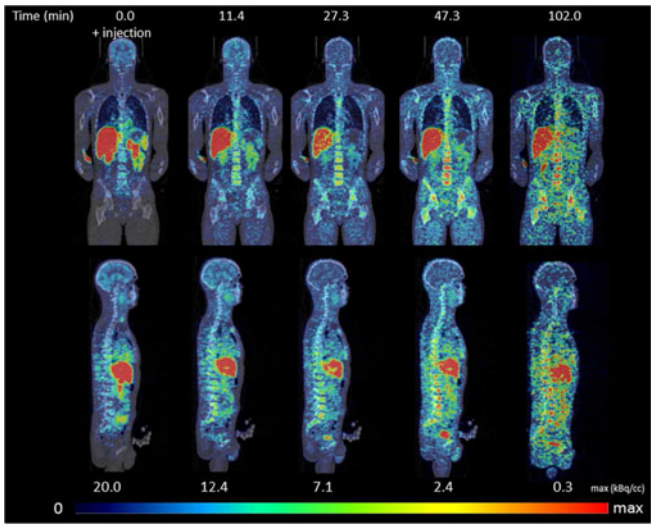

Fig. 1. Whole-body coronal and mid-sagittal PET–CT sections of [^{11}C]-NE40 in subject 2 (uncorrected for decay, in kBq/cc). Data are normalized in the same scale on a maximum activity given in the *bottom row*, in order to better visualize the relative distribution. *Top row* indicates start time (min) of whole-body scan.

through the urinary tract, with a biological urinary clearance half-life estimated at 183±96 h. Due to the slow urinary excretion rate, collected urinal activity from the first two patients during 3 h post-injection was very limited and therefore was not further taken into account for the calculations. Rapid uptake (to a maximum of 1.5–3 % of the injected activity) and fast washout in the brain were seen, in accordance with the low CB2R expression levels in the normal brain.

Figure 2 shows relative time–activity curves for the liver, brain, gallbladder, and spleen after injection of [^{11}C]-NE40. The highest variability in activity was observed in the gallbladder. In one of the subjects, we observed an early decrease of the gallbladder activity, with a second peak towards 50 min post-injection.

Time-integrated activity coefficients for all individual patients and source organs are given in Supplementary

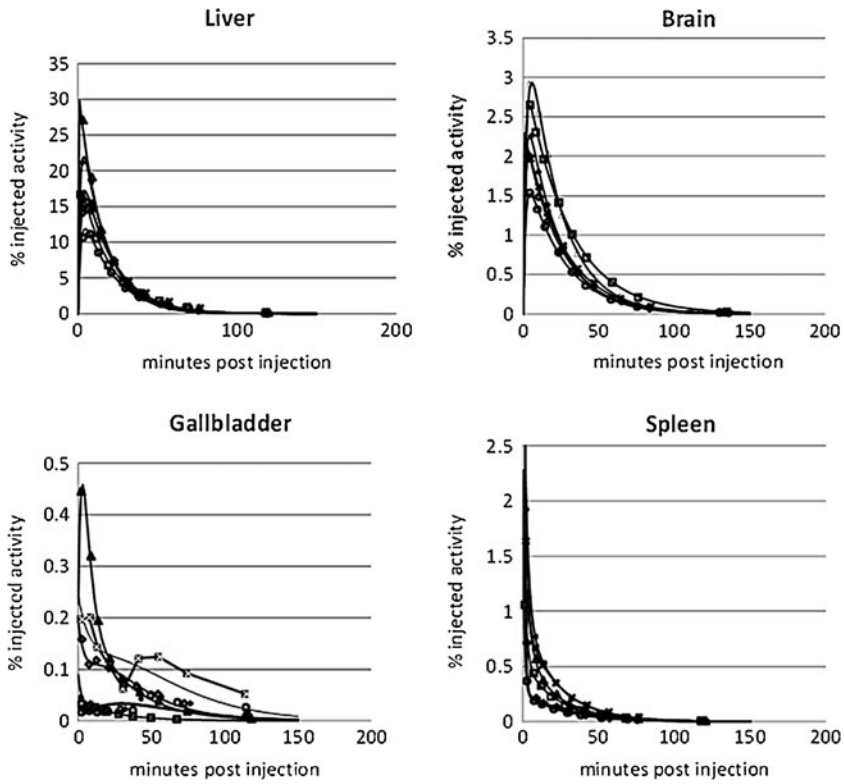

Fig. 2. Mean activity over time in the brain, spleen, liver, and gallbladder as a fraction of total-body activity for all subjects.

Table 2. Radiation absorbed dose estimate (OLINDA) based on the ICRP 30 gastrointestinal tract model

Target organ	Mean absorded dose (μGy/MBq)	Coefficient of variation (%)
Adrenals	2.7±0.4	14.1
Brain	2.7±0.8	30.7
Breasts	1.5±0.3	20.1
Gallbladder wall	5.8±0.1	21.8
Lower large intestine wall	2.6±0.1	38.8
Small intestine	15.6±1.0	65.7
Stomach wall	2.3±0.5	22.8
Upper large intestine wall	6.7±3.8	57.6
Heart wall	7.0±2.3	32.4
Kidneys	6.7±1.5	23.0
Liver	11.5±1.2	10.0
Lungs	4.0±0.7	17.2
Muscle	1.8±0.4	23.4
Pancreas	2.7±0.4	15.8
Red marrow	5.1±0.9	18.4
Osteogenic cells	4.3±1.0	23.4
Skin	1.3±0.3	23.5
Spleen	6.0±1.3	21.8
Testes	1.4±0.4	25.2
Thymus	1.8±0.3	19.3
Thyroid	4.3±1.3	30.9
Urinary bladder wall	2.4±0.8	31.2
Uterus	2.8±1.1	39.7
Total body	2.4±0.5	21.3
Effective dose (μSv/MBq)	3.6±0.8	22.3

Data are mean±SD

Table 1. Table 2 summarizes organ mean radiation absorbed doses and the effective doses. Individual organ absorbed doses and average organ doses derived from individual doses as well as based on mean kinetic parameters (time-integrated activity coefficient) and their relative difference (%) are given in Supplementary Table 2. As can be seen from this table, there is only a very small difference between both approaches. The small intestine and the liver showed the highest organ dose of 15.6 and 11.5 μGy/MBq, respectively, followed by the heart wall (7.02 μGy/MBq). Table 1 includes the individual ED estimates for all subjects. The average ED was 3.64±0.81 μSv/MBq (range 2.79 to 5.09 μSv/MBq). No significant correlation between age and ED was found.

Figure 3 shows the time activity curves (SUV) with activity values corrected for decay caused by the time interval between tracer injection and start time of the different whole-body PET scans of the six healthy volunteers for the brain and spleen. In the brain, a maximum between 10–20 min can be seen in some subjects, with thereafter a continuous decline of the SUV value. In the spleen, after 20 min a stable SUV is seen, plateauing around 1.

Discussion

Biomarkers of (neuro)inflammation can be useful as a tool in drug development and in clinical conditions for severity assessment and therapy follow-up. The CB2R is predominantly expressed in peripheral tissues and shows the highest expression levels in organs of the immune system [34]. In the central nervous system, CB2R is upregulated in inflammatory conditions of activated microglia. Most of the CB2R radioligands described so far are derivatives of the 2-oxoquinoline class that have shown a high selectivity for CB2Rs as inverse agonists [22–24, 35, 36]. Although some were promising in *in vitro* studies, their *in vivo* stability was poor with fast metabolization. Proof-of-principle of the feasibility of CB2R imaging in pathological conditions with a neuroinflammatory component *in vivo* was described by Horti et al. [21]. Since [^{11}C]-NE40 showed favorable characteristics for neuroimaging, we performed this first-in-man study to assess the biodistribution and evaluate the safety of [^{11}C]-NE40.

The gallbladder showed the highest variability in activity. In one of the subjects, there is an early decrease of the gallbladder activity, with a second peak towards 50 min post-injection, possibly due to an early contraction of the gallbladder, after which there is an accumulation of the activity with a second contraction. Overall, the gallbladder activity can differ between subjects due to large differences in the individual kinetics of gallbladder emptying, a process influenced by multiple hormonal factors and gastrointestinal interactions.

The average injected tracer mass dose in this study was less than 1.0 μg. There were no subjective effects or adverse

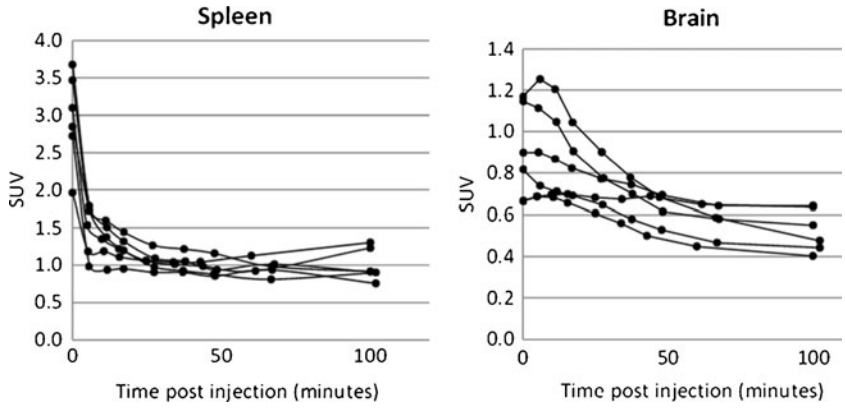

Fig. 3. Time–activity curves (expressed in SUV; activity values decay-corrected relative to the time of tracer injection) of the spleen and brain for the six volunteers.

events including changes in laboratory blood tests, blood pressure, pulse, and ECG. The subjects in this study received a total ED of 2.1 mSv including the PET and attenuation correction CT studies. In a recent literature overview of 32 human PET radiation dosimetry studies with ^{11}C radioligands, van der Aart et al. showed that the vast majority have an effective dose of below 9 μSv/MBq, with a mean of 5.9 μSv/MBq [37]. The effective radiation dose in our study is thus less than this average, moreover indicating that multiple PET scans can be performed in the same subject within conventionally accepted dose limits (class IIA WHO of 10 mSv), allowing its use in drug development and follow-up studies.

Conclusion

[^{11}C]-NE40 results in an effective human radiation dose of 3.64 μSv/MBq, which is in the lower end of the range of ^{11}C tracers. The biodistribution with spleen uptake and absence of fixed brain uptake in healthy conditions makes the tracer promising for further studies in pathological conditions.

Acknowledgments. Financial support of the European Commission (FP7/2007-2013, INMiND, grant agreement no. 278850) is gratefully acknowledged. We also thank Kwinten Porters, Mieke Steukers, Tjibbe De Groot, Marva Bex, and Lena Sojka for their contribution.

Conflict of Interest. The authors have no conflicts of interest.

References

1. Munro S, Thomas KL, Abu-Shaar M (1993) Molecular characterization of a peripheral receptor for cannabinoids. Nature 365:61–65
2. Felder CC, Joyce KE, Briley EM et al (1995) Comparison of the pharmacology and signal transduction of the human cannabinoid CB1 and CB2 receptors. Mol Pharmacol 48:443–450
3. Lynn AB, Herkenham M (1994) Localization of cannabinoid receptors and nonsaturable high-density cannabinoid binding sites in peripheral tissues of the rat: implications for receptor-mediated immune modulation by cannabinoids. J Pharmacol Exp Ther 268:1612–1623
4. Prestifilippo JP, Fernandez-Solari J, de la Cal C et al (2006) Inhibition of salivary secretion by activation of cannabinoid receptors. Exp Biol Med (Maywood) 231:1421–1429
5. Cavuoto P, McAinch AJ, Hatzinikolas G, Janovska A, Game P, Wittert GA (2007) The expression of receptors for endocannabinoids in human and rodent skeletal muscle. Biochem Biophys Res Commun 364:105–110
6. Bermudez-Silva FJ, Suarez J, Baixeras E et al (2008) Presence of functional cannabinoid receptors in human endocrine pancreas. Diabetologia 51:476–487
7. El-Talatini MR, Taylor AH, Elson JC, Brown L, Davidson AC, Konje JC (2009) Localisation and function of the endocannabinoid system in the human ovary. PLoS One 4:e4579
8. Liu QR, Pan CH, Hishimoto A et al (2009) Species differences in cannabinoid receptor 2 (CNR2 gene): identification of novel human and rodent CB2 isoforms, differential tissue expression and regulation by cannabinoid receptor ligands. Genes Brain Behav 8:519–530
9. Onaivi ES (2006) Neuropsychobiological evidence for the functional presence and expression of cannabinoid CB2 receptors in the brain. Neuropsychobiology 54:231–246
10. Van Sickle MD, Duncan M, Kingsley PJ et al (2005) Identification and functional characterization of brainstem cannabinoid CB2 receptors. Science 310:329–332
11. Ehrhart J, Obregon D, Mori T et al (2005) Stimulation of cannabinoid receptor 2 (CB2) suppresses microglial activation. J Neuroinflammation 2:29
12. Curto-Reyes V, Llames S, Hidalgo A, Menendez L, Baamonde A (2010) Spinal and peripheral analgesic effects of the CB2 cannabinoid receptor agonist AM1241 in two models of bone cancer-induced pain. Br J Pharmacol 160:561–573
13. Bisogno T, Di Marzo V (2008) The role of the endocannabinoid system in Alzheimer's disease: facts and hypotheses. Curr Pharm Des 14:2299–3305
14. Pazos MR, Sagredo O, Fernandez-Ruiz J (2008) The endocannabinoid system in Huntington's disease. Curr Pharm Des 14:2317–2325
15. Benito C, Nunez E, Tolon RM et al (2003) Cannabinoid CB2 receptors and fatty acid amide hydrolase are selectively overexpressed in neuritic plaque-associated glia in Alzheimer's disease brains. J Neurosci 23:11136–11141
16. Palazuelos J, Aguado T, Pazos MR et al (2009) Microglial CB2 cannabinoid receptors are neuroprotective in Huntington's disease excitotoxicity. Brain 132:3152–3164
17. Price DA, Martinez AA, Seillier A et al (2009) WIN55,212-2, a cannabinoid receptor agonist, protects against nigrostriatal cell loss in the 1-methyl-4-phenyl-1,2,3,6-tetrahydropyridine mouse model of Parkinson's disease. Eur J Neurosci 29:2177–2186
18. Burns HD, Van Laere K, Sanabria-Bohorquez S et al (2007) [18F]MK-9470, a positron emission tomography (PET) tracer for *in vivo* human PET brain imaging of the cannabinoid-1 receptor. Proc Natl Acad Sci USA 104:9800–9805
19. Donohue SR, Varnas K, Jia Z, Gulyas B, Pike VW, Halldin C (2009) Synthesis and *in vitro* autoradiographic evaluation of a novel high-affinity radioiodinated ligand for imaging brain cannabinoid subtype-1 receptors. Bioorg Med Chem Lett 19:6209–6212
20. Horti AG, Van Laere K (2008) Development of radioligands for *in vivo* imaging of type 1 cannabinoid receptors (CB1) in human brain. Curr Pharm Des 14:3363–3383
21. Horti AG, Gao Y, Ravert HT et al (2010) Synthesis and biodistribution of [11C]A-836339, a new potential radioligand for PET imaging of cannabinoid type 2 receptors (CB2). Bioorg Med Chem 18:5202–5207
22. Evens N, Bosier B, Lavey BJ et al (2008) Labelling and biological evaluation of [(11)C]methoxy-Sch225336: a radioligand for the cannabinoid-type 2 receptor. Nucl Med Biol 35:793–800
23. Gao M, Wang M, Miller KD, Hutchins GD, Zheng QH (2010) Synthesis and *in vitro* biological evaluation of carbon-11-labeled quinoline derivatives as new candidate PET radioligands for cannabinoid CB2 receptor imaging. Bioorg Med Chem 18:2099–2106
24. Evens N, Muccioli GG, Houbrechts N et al (2009) Synthesis and biological evaluation of carbon-11- and fluorine-18-labeled 2-oxoquinoline derivatives for type 2 cannabinoid receptor positron emission tomography imaging. Nucl Med Biol 36:455–465
25. Evens N, Vandeputte C, Coolen C et al (2012) Preclinical evaluation of [11C]NE40, a type 2 cannabinoid receptor PET tracer. Nucl Med Biol 39:389–399
26. Ames BN, McCann J, Yamasaki E (1975) Methods for detecting carcinogens and mutagens with the Salmonella/mammalian-microsome mutagenicity test. Mutat Res 31:347–364
27. Evens N, Vandeputte C, Muccioli GG et al (2011) Synthesis, *in vitro* and *in vivo* evaluation of fluorine-18 labelled FE-GW405833 as a PET tracer for type 2 cannabinoid receptor imaging. Bioorg Med Chem 19:4499–4505
28. Lassmann M, Chiesa C, Flux G, Bardies M, Committee ED (2011) EANM Dosimetry Committee guidance document: good practice of clinical dosimetry reporting. Eur J Nucl Med Mol Imaging 38:192–200
29. Van Laere K, Koole M, Sanabria Bohorquez SM et al (2008) Whole-body biodistribution and radiation dosimetry of the human cannabinoid type-1 receptor ligand 18F-MK-9470 in healthy subjects. J Nucl Med 49:439–445
30. Bolch WE, Eckerman KF, Sgouros G, Thomas SR (2009) MIRD pamphlet no. 21: a generalized schema for radiopharmaceutical dosimetry—standardization of nomenclature. J Nucl Med 50:477–484
31. ICoR Protection (1979) Limits for intakes of radionuclides by workers. Pergamon Press, New York
32. Cloutier RJ, Smith SA, Watson EE, Snyder WS, Warner GG (1973) Dose to the fetus from radionuclides in the bladder. Heal Phys 25:147–161
33. ICRP (1991) ICRP Publication 60: recommendations of the International Commission on Radiological Protection. Pergamon Press, Oxford

34. Maccarrone M, Battista N, Centonze D (2007) The endocannabinoid pathway in Huntington's disease: a comparison with other neurodegenerative diseases. Prog Neurobiol 81:349–379
35. Raitio KH, Savinainen JR, Nevalainen T, Jarvinen T, Vepsalainen J (2006) Synthesis and *in vitro* evaluation of novel 2-oxo-1,2-dihydroquinoline CB2 receptor inverse agonists. Chem Biol Drug Des 68:334–340
36. Turkman N, Shavrin A, Paolillo V et al (2012) Synthesis and preliminary evaluation of [18F]-labeled 2-oxoquinoline derivatives for PET imaging of cannabinoid CB2 receptor. Nucl Med Biol 39:593–600
37. van der Aart J, Hallett WA, Rabiner EA, Passchier J, Comley RA (2012) Radiation dose estimates for carbon-11-labelled PET tracers. Nucl Med Biol 39:305–314